Available online at www.sciencedirect.com
ScienceDirect
International Journal of Multiphase Flow 33 (2007) 638–657
International Journal of Multiphase Flow
www.elsevier.com/locate/ijmulflow

Interfacial drag of two-phase flow in porous media

Werner Schmidt

AREVA NP, P.O. Box 3220, D 91050 Erlangen, Germany

Received 30 May 2005; received in revised form 14 September 2006

Abstract

In this paper, the influence of the interfacial drag on the pressure loss of combined liquid and vapour flow through particulate porous media is investigated. Motivation for this is the coolability of fragmented corium which may be expected during a severe accident in a nuclear power plant. Cooling water is evaporated due to the particles decay heat. To reach coolability, the outflowing steam has to be replaced by inflowing water.

The pressure loss for the resulting two-phase flow through the debris is determined by the friction forces at the particles as well as at the interfacial drag between the fluids. In return, the resulting pressure field influences the coolant inflow through the boundaries and thus the coolability of the fragments.

Starting from commonly used friction correlations, it is shown that only those with explicit consideration of the interfacial drag can represent the pressure loss. Enhancements for the formulation of the interfacial drag are proposed. This modified model fits experimental data of isothermal air/water experiments as well as data of boiling particle beds.

Keywords: Porous media; Two-phase flow; Interfacial friction; Coolability; Severe accident

1. Introduction

Multiphase flow in porous media is of central concern in various scientific and technical fields. In many of these applications a liquid phase and a gaseous phase, mostly vapour, have to be considered. For example, in the frame of nuclear reactor safety analyses, the coolability of fragmented corium is of central interest. Particle diameters d_p from 1 to 6 mm and porosities ε of about 0.4 have to be assumed in this application. Due to the corium decay heat water is evaporated and the produced steam rises to the top. A steady state, and thus coolability, is reached if the produced steam can be discharged and the evaporated water is replaced by infiltration. In a pure 1D configuration with a water reservoir on top of the porous bed, the up-flowing steam and the down-flowing water are in counter-current flow configuration. A limit of coolability, corresponding to the dry-out heat flux (DHF), is determined by the counter-current flooding limit for this flow pattern. A significantly higher DHF is reached if at least some fraction of the water can flow into the porous bed via the bottom. This requires less water influx from the top, enabling higher steam fluxes and thus an increased DHF. The two

E-mail address: werner.schmidt@areva.com

0301-9322/$ - see front matter
doi:10.1016/j.ijmultiphaseflow.2006.09.006

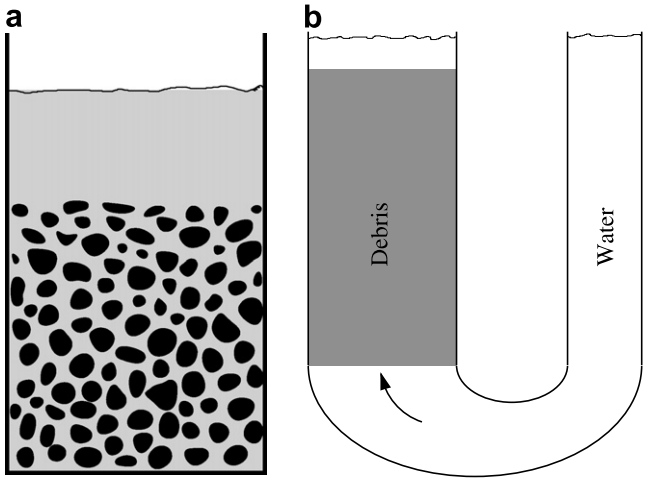

Fig. 1. One-dimensional geometries.

situations are sketched in Fig. 1. For realistic multidimensional configurations in a water environment facilitated water flow paths to bottom regions support coolability, similar to Fig. 1b.

As this discussion already shows, the DHF is determined by the friction laws for the flow in the porous particle bed. The motion of the fluids is hindered by the friction at the non-movable solid structures as well as by the existence of the other phase. The interfacial drag affects the DHF negatively in the counter-current flow pattern, but supports the water inflow from below in co-current mode. Thus, the investigation of the interfacial drag is the central concern of this paper. Consequences on the coolability of realistic multidimensional configurations are investigated in Schmidt (2004).

2. The friction laws

2.1. Classical models without explicit consideration of interfacial friction

A simplified formulation of the momentum conservation equations can be deduced from the pressure loss of fluids in porous media. This pressure loss can be calculated by the Ergun equation (Ergun, 1952). The characteristics of the porous media are considered in the parameters permeability K and passability η. To include the impact of the smaller effective cross section for two phase flow these parameters have to be extended by a function depending on the volume fraction. In these relative permeabilities and passabilities the mutual influence of the fluid phases on the pressure loss is included. This yields

$$\text{Liquid:} \quad -\nabla p_{\mathrm{L}} = -\varrho_{\mathrm{L}}\vec{g} + \frac{\mu_{\mathrm{L}}}{KK_{\mathrm{rL}}(\alpha)}\vec{j}_{\mathrm{L}} + \frac{\varrho_{\mathrm{L}}}{\eta\eta_{\mathrm{rL}}(\alpha)}|\vec{j}_{\mathrm{L}}|\vec{j}_{\mathrm{L}}\left(-\frac{\vec{F}_{\mathrm{i}}}{1-\alpha}\right), \tag{1}$$

$$\text{Vapour:} \quad -\nabla p_{\mathrm{G}} = -\varrho_{\mathrm{G}}\vec{g} + \frac{\mu_{\mathrm{G}}}{KK_{\mathrm{rG}}(\alpha)}\vec{j}_{\mathrm{G}} + \frac{\varrho_{\mathrm{G}}}{\eta\eta_{\mathrm{rG}}(\alpha)}|\vec{j}_{\mathrm{G}}|\vec{j}_{\mathrm{G}}\left(+\frac{\vec{F}_{\mathrm{i}}}{\alpha}\right). \tag{2}$$

Here ϱ and μ are the density and dynamic viscosity of the liquid phase (index L) and the gaseous phase (index G), respectively. The superficial velocity of the fluids is given by j and ∇p is the pressure gradient. α denotes the void fraction. The terms given in brackets indicate the interfacial drag that is not considered in the classical models. According to Ergun the porous media parameters K and η can be calculated by

$$K = \frac{\epsilon^3 d_{\mathrm{p}}^2}{A(1-\epsilon)^2} \quad \text{and} \quad \eta = \frac{\epsilon^3 d_{\mathrm{p}}}{B(1-\epsilon)}, \tag{3}$$

where the Ergun constants A and B can be taken from pressure loss measurements in granular debris. Usually $A = 150$ and $B = 1.75$ are used.

Several approaches for the relative permeability K_r and passability η_r, based on dryout heat flux experiments, can be found in the literature. The most commonly used approach has the form

$$K_{rG}(\alpha) = \alpha^n, \quad \eta_{rG}(\alpha) = \alpha^m, \tag{4}$$

$$K_{rL}(\alpha) = (1-\alpha)^n, \quad \eta_{rL}(\alpha) = (1-\alpha)^m. \tag{5}$$

Lipinski (1981) used $K_r = \beta^3$ (β = phase fraction in the pores) and assumed the same exponent for the relative passability $\eta_r = \beta^3$. Based on his own dryout experiments that yielded a smaller dryout heat flux, Reed (1982) proposed an exponent $m = 5$ for the relative passabilities. This exponent was also used by Lipinski in later publications (1984). The dryout heat flux calculated with this approach fits well with the experimental values for top fed particulate bed configurations.

Usually the measuring procedure was iterative. The critical heat flux was determined by increasing the bed power and observing the largest value before the temperature in any part of the bed starts to rise (local dryout). Hu and Theofanous (1991) criticised this measurement method, and explained that the resulting dryout heat flux values would be too high, because the power was increased further before the dryout was detected. Additionally, they pointed out that in most of the experiments the ratio of the test section diameter to the particle size was too small, yielding an increased water inflow along the walls. So, they proposed an exponent $m = 6$ to increase the friction between the fluids and the particles, yielding a smaller dryout heat flux. A summary of the classical models is given in Table 1.

2.2. Models including explicit interfacial friction

As Tutu et al. (1984) had already pointed out in his isothermal air/water experiments, an explicit consideration of the interfacial friction is necessary. He used a one dimensional test column filled with stainless steel spheres. A defined air mass-flow was injected into the water filled test section from below. The pressure loss inside the bed was measured. Additionally, the level swell of the water may be used to determine the void fraction inside the bed. As there is no net water flow ($j_L = 0$), Eq. (1) for the liquid phase without interfacial friction directly yields, that the pressure gradient will always be the hydrostatic head, independent from the gas flow. But the measurements of the pressure gradient showed a significantly smaller value than the hydrostatic one. This directly indicates the influence of the interfacial friction. The experiment and the results will be discussed in detail in Section 3.1.

2.2.1. The model of Schulenberg and Müller

Based on similar experiments, Schulenberg and Müller (1986) correlated their data and deduced an equation for the interfacial friction from the measured pressure loss equation (1)

$$F_i = 350(1-\alpha)^7 \alpha \frac{\varrho_L K}{\eta\sigma}(\varrho_L - \varrho_G) g \left(\frac{j_G}{\alpha} - \frac{j_L}{(1-\alpha)}\right)^2. \tag{6}$$

Here σ is the surface tension. Inserting this formulation for the interfacial drag into the vapour equation and assuming a relative permeability of $K_{rG} = \alpha^3$, they determined the relative passability η_{rG} for the vapour phase. For the liquid phase they assumed the same exponents as Reed. Their result is

Table 1
Relative permeability K_r and passability η_r in the classical formulations

	K_{rG}	η_{rG}	K_{rL}	η_{rL}
Lipinski	α^3	α^3	$(1-\alpha)^3$	$(1-\alpha)^3$
Reed	α^3	α^5	$(1-\alpha)^3$	$(1-\alpha)^5$
Hu/Theofanous	α^3	α^6	$(1-\alpha)^3$	$(1-\alpha)^6$

$$K_{rG}(\alpha) = \alpha^3, \quad \eta_{rG}(\alpha) = \begin{cases} 0.1\alpha^4 & : \alpha \leqslant 0.3, \\ \alpha^6 & : \alpha > 0.3, \end{cases} \tag{7}$$

$$K_{rL}(\alpha) = (1-\alpha)^3, \quad \eta_{rL}(\alpha) = (1-\alpha)^5. \tag{8}$$

2.2.2. The model of Tung and Dhir

A completely different approach has been proposed by Tung and Dhir (1988). Based on visual observation in air/water flow experiments, they defined flow pattern ranges for bubbly, slug and annular flow. Besides a subpattern in the bubbly flow regime, only relevant for particle sizes greater than 12 mm, the flow pattern limits are given in Table 2. The transition between the patterns is defined via a weighting function.

Based on the definition of the permeability K and passability η in Eq. (3), Tung and Dhir used geometrical arguments, and inserted an effective porosity and particle diameter that is seen by the gas flow. This guided them to the following formulation for the relative permeability and passability of the gas for the different flow patterns:

Particle gas drag F_{pG}

$0 \leqslant \alpha \leqslant \alpha_3$ (bubbly and slug flow)

$$K_{rG} = \left(\frac{1-\varepsilon}{1-\varepsilon\alpha}\right)^{4/3}\alpha^4 \quad \text{and} \quad \eta_{rG} = \left(\frac{1-\varepsilon}{1-\varepsilon\alpha}\right)^{2/3}\alpha^4, \tag{9}$$

$\alpha_3 \leqslant \alpha \leqslant 1$ (pure annular flow)

$$K_{rG} = \left(\frac{1-\varepsilon}{1-\varepsilon\alpha}\right)^{4/3}\alpha^3 \quad \text{and} \quad \eta_{rG} = \left(\frac{1-\varepsilon}{1-\varepsilon\alpha}\right)^{2/3}\alpha^3. \tag{10}$$

Similar ideas for the liquid part are based on the visual observation that the liquid is always in contact with the particles like a film. Thus, they left the particle diameter unchanged and only included an effective volume fraction. By this they deduced

Particle liquid drag F_{pL}

$$K_{rL} = \eta_{rL} = (1-\alpha)^4. \tag{11}$$

It has to be noted, that the above given exponent is increased from 3 to 4 compared to the original paper, because the momentum equationss (1) and (2) are divided by the volume fraction in this work, in contrast to Tung and Dhir (1988).

Interfacial drag F_i

In addition to the drag at the solid matrix, Tung and Dhir also deduced a correlation for the liquid/vapour interfacial friction F_i. For bubbly and slug flow, this drag force is based on an expression for the drag on a single bubble or slug, multiplied by the number of bubbles or slugs per unit volume. A detailed description can be found in the original paper of Tung and Dhir (1988). Here only the results will be given

Table 2
Flow regime bounds of the Tung/Dhir model

		Bubbly flow
α_1	$\min(0.3,\ 6(1-\gamma)^2)$	
		Transition
α_2	$\pi/6 \approx 0.52$	
		Slug flow
α_3	0.6	
		Transition
α_4	$\pi\sqrt{2}/6 \approx 0.74$	
		Annular flow

$$F_i = C_1 \frac{\mu_L}{D_b^2 \varepsilon}(1-\alpha) j_r + C_2 \frac{((1-\alpha)\varrho_L + \alpha \varrho_G)}{D_b \varepsilon^2}(1-\alpha)^2 |j_r| j_r. \tag{12}$$

The relative velocity j_r is given by

$$j_r = \frac{j_G}{\alpha} - \frac{j_L}{(1-\alpha)}. \tag{13}$$

Based on visual observations the bubble diameter D_b is defined by

$$D_b = 1.35 \sqrt{\frac{\sigma}{g(\varrho_L - \varrho_G)}}. \tag{14}$$

The friction coefficients C_1 and C_2 are given separately for bubbly and slug flow

$0 \leqslant \alpha \leqslant \alpha_1$ (bubbly flow)

$$C_1 = 18\alpha \quad \text{and} \quad C_2 = 0.34(1-\alpha)^3 \alpha, \tag{15}$$

$\alpha_2 \leqslant \alpha \leqslant \alpha_3$ (slug flow)

$$C_1 = 5.21\alpha \quad \text{and} \quad C_2 = 0.92(1-\alpha)^3 \alpha, \tag{16}$$

$\alpha_4 \leqslant \alpha \leqslant 1$ (pure annular flow).

In the annular flow regime the interfacial drag can be modeled in a manner similar to the particle-gas drag, by using the relative velocity between the gas and the liquid. This yields

$$F_i = \frac{\mu_G}{K K_{rG}}(1-\alpha) j_r + (1-\alpha)\alpha \frac{\varrho_G}{\eta \eta_{rG}} |j_r| j_r. \tag{17}$$

The relative permeability and passability to be inserted here are the same as for the gas-particle drag and are given in Eq. (9).

2.2.3. Modifications of the Tung/Dhir model

Tung and Dhir compared their model to the measured pressure gradients, as well as the void fractions of the isothermal air/water experiments of Chu et al. (1983). They found a good agreement with the experimental data. But, Chu et al. used relatively large particles of $d_p = 5.8$ mm, $d_p = 9.9$ mm and $d_p = 19$ mm. As lcould be seen previously in the paper of Tung and Dhir (1988) for the $d_p = 5.8$ mm data, their model shows greater deviations for smaller particles. Looking at the diameter of the gas bubbles used by Tung land Dhir, this discrepancy can easily be understood. Inserting the density difference between air and liquid as well as the surface tension into Eq. (14) yields a bubble diameter of $D_b = 3.75$ mm. So, the applied bubble diameter becomes larger then the pores for small particles, in contradiction to the geometric ideas of the model. Additionally, the assumption of gas bubbles in the pores becomes questionable for small particles. This must lead to some modifications of the original Tung/Dhir model to extend it to smaller particle diameters.

The first central point to be modified is the diameter of the gas bubbles or the slugs. This diameter strongly influences the interfacial drag in bubbly and slug flow, as could be seen in Eq. (12). Based on the assumption of a cubic arrangement of spherical particles a maximum diameter of $D_{b_{max}} = d_p(\sqrt{2}-1)$ may be deduced for a bubble. To make a connection with the original Tung/Dhir model, a modified bubble diameter is simply defined by

$$D_b^m = \min\left(1.35\sqrt{\frac{\sigma}{g(\varrho_L - \varrho_G)}}, 0.41 d_p\right). \tag{18}$$

The second point to be modified are the flow pattern ranges used in the model. The original bounds are given as dashed lines in Fig. 2.

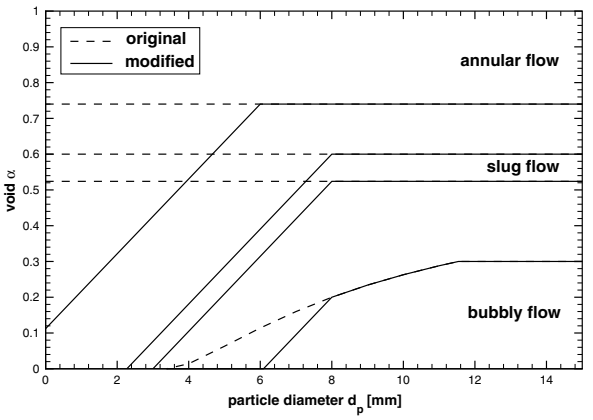

$$\alpha_1^m = \begin{cases} \frac{\pi/6}{5}(d_p - 8\,\mathrm{mm}) + \alpha_1 & : d_p < 8\,\mathrm{mm} \\ \alpha_1 & : d_p > 8\,\mathrm{mm} \end{cases}$$

$$\alpha_2^m = \begin{cases} \frac{\pi/6}{5}(d_p - 8\,\mathrm{mm}) + \alpha_2 & : d_p < 8\,\mathrm{mm} \\ \alpha_2 & : d_p > 8\,\mathrm{mm} \end{cases}$$

$$\alpha_3^m = \begin{cases} \frac{\pi/6}{5}(d_p - 8\,\mathrm{mm}) + \alpha_3 & : d_p < 8\,\mathrm{mm} \\ \alpha_3 & : d_p > 8\,\mathrm{mm} \end{cases}$$

$$\alpha_4^m = \begin{cases} \frac{\pi/6}{5}(d_p - 6\,\mathrm{mm}) + \alpha_4 & : d_p < 6\,\mathrm{mm} \\ \alpha_4 & : d_p > 6\,\mathrm{mm} \end{cases}$$

Fig. 2. Flow pattern map for the modified Tung/Dhir model.

As can be seen, for particle diameters less then 3 mm, no pure bubbly flow is expected. This fits the usual understanding. But, in this work an even steeper reduction of the bubbly flow regime with decreasing particle diameter is proposed. On the other hand, annular flow in the picture of Tung and Dhir is by gas tubes wiggleing along the pores. For small particles this "tube picture" becomes questionable. Now, in the annular flow regime, fixed gas channels in the order of the particle size may establish. Inside a representative control volume, including on average several pores, annular flow may establish even for smaller void fractions. This is also conform to the flow pattern observations characterised by Haga et al. (2000) using tracer particles. They reported a channel like configuration for 2 mm spheres down to a void fraction of $\alpha = 0.3$. So, an enlargement of the annular flow range for particles less than 6 mm is proposed here. Consequently, the bounds for the slug flow regime also have to be modified, e.g. slugs will prefer flow paths in the wake of predecessors yielding less interfacial drag than for independent slugs. The modifications to the flow pattern bounds are also given in Fig. 2 by the solid lines.

Additionally, further modifications to the interfacial drag in the annular flow regime are necessary. As already discussed above, for smaller particles a channel like flow establishes already for smaller void fractions. Compared to the classical picture of Tung and Dhir, the interfacial area between gas and liquid now is reduced. This motivates a decrease of the drag for decreasing particle diameter. By adaptation to the experimental results of Tutu et al. (1984), discussed in detail in the next chapter, a multiplicative factor of $(d_\mathrm{p}/6\times10^{-3})^2$ is proposed for particles smaller than 6 mm in this work. Additionally, as can be seen in the formulation of the friction term for annular flow in Eq. (17), this drag decreases linearly to zero when the void fraction reaches the limit $\alpha \to 1$. This decrease seems to be too weak compared to usual correlations. So, in this work an additional multiplier of $(1-\alpha)^2$ is proposed to obtain a more realistic decrease of the interfacial drag in the annular flow regime for increasing void fraction. This leads to the following modified formulation of the interfacial friction in the annular flow regime:

$$F_\mathrm{i}^m = \left(\frac{\mu_\mathrm{G}}{KK_\mathrm{rG}}(1-\alpha)j_\mathrm{r} + (1-\alpha)\alpha\frac{\varrho_\mathrm{G}}{\eta\eta_\mathrm{rG}}|j_\mathrm{r}|j_\mathrm{r}\right) * (1-\alpha)^2 \begin{cases} \left(\frac{d_\mathrm{p}}{6\times10^{-3}}\right)^2 & : d_\mathrm{p} < 6\,\mathrm{mm} \\ 1 & : d_\mathrm{p} > 6\,\mathrm{mm} \end{cases} \tag{19}$$

All the modifications proposed above influence mainly the formulation of the interfacial drag. As will be seen in the next chapter, it is in general not easy to separate the different friction contributions in the experiments. Interfacial and particle drag are superimposed, but can be separated for specific conditions with no net water flow. On the other hand, for boiling beds – as in the reactor application – this splitting is not possible. Comparisons to experiments with boiling beds will also be given in the next chapter. As will be seen, especially the DEBRIS experiments described in Section 3.2.1 support the above proposed modifications of the interfacial drag.

3. Comparison of the friction laws with experimental data

3.1. Comparison to isothermal air/water flow experiments

Isothermal air/water experiments are a good method to investigate the friction laws of two phase flow in porous media with a simple experimental setup. By fixing the water and air flow rates through a vertical test column filled with particles, defined steady state conditions, either for co- or for counter-current flow, may be established. As the gas flow rate from the bottom to the top is fixed, a constant void fraction will establish over the whole bed height. Therefore, the capillary pressure will be constant and its gradient is zero. So, the same pressure gradient acts on both fluids. This pressure gradient in the test column can easily be measured. Additionally, the void fraction in the bed can be determined, either by visual observation through transparent vessel walls, or by the change of the water level on the top.

The experimental data can be compared to theoretical results of the models to verify the friction laws. For this, the momentum conservation Eqs. (1) and (2) will be used in a dimensionless form. Dividing by $g\varepsilon(\varrho_L - \varrho_G)$ yields

$$(1-\alpha)P^\star = (1-\alpha)\frac{\varrho_L g}{g(\varrho_L - \varrho_G)} + F^\star_{pL} - F^\star_i \tag{20}$$

$$\alpha P^\star = \alpha\frac{\varrho_G g}{g(\varrho_L - \varrho_G)} + F^\star_{pG} + F^\star_i \tag{21}$$

with

$$P^\star = \frac{-\nabla p}{g(\varrho_L - \varrho_G)}, \quad F^\star = \frac{F}{g\varepsilon(\varrho_L - \varrho_G)}. \tag{22}$$

The two friction terms of the particle–fluid drag are combined in the force F_p. Eliminating the normed pressure gradient $P^\star$ yields

$$\alpha(1-\alpha) + \alpha F^\star_{pL} - (1-\alpha)F^\star_{pG} - F^\star_i = 0. \tag{23}$$

Inserting the friction laws presented in the previous chapter then gives an equation with the three unknowns j_G, j_L and α. Fixing one velocity, usually the liquid one, and varying the void fraction the other velocity can be calculated easily by selecting the physically relevant root. Additionally, adding the two Eqs. (20) and (21) yields an equation for the pressure gradient

$$P^\star = \frac{(1-\alpha)\varrho_L + \alpha\varrho_G}{\varrho_L - \varrho_G} + F^\star_{pL} + F^\star_{pG}. \tag{24}$$

So, sets of j_G, j_L, $P^\star$ and α may be calculated that directly can be compared with the experimental values.

A comparison of calculated results with experimental air/water data measured by Tutu et al. (1984) is shown in Figs. 3 and 4. Air was injected into the bottom of a water filled test column of stainless steel spheres ($d_p = 6.35$ mm). The superficial velocity of the air, corresponding to the mass flux through the test column, was varied. For the established steady states the pressure gradient was measured by the difference of two pressure taps. In Fig. 3 the dimensionless pressure gradient is plotted as function of the superficial velocity of the gas. The figure shows that the pressure gradient becomes less than one, indicating a pressure loss due to the gas flow. The classical models, which do not explicitly consider the interfacial friction, cannot reproduce this behaviour. This can already be seen in Eq. (20). As there is no net water flow the superficial velocity $j_L = 0$ leads to $F^\star_{pL} = 0$. With $F^\star_i = 0$ this yields $P^\star = \varrho_L/(\varrho_L - \varrho_G) \approx 1$ independent of the gas mass flux. So, in these models the pressure field must always be equal to the hydrostatic pressure, and is not influenced by the gas flux.

This behaviour is not verified by the experimental data. The measured pressure first decreases with increasing gas flow rate, although the water is still the continuous phase. This can only be explained by including the drag of the up-flowing gas on the liquid. The models of Schulenberg and Tung/Dhir, which including the interfacial friction, show this characteristic qualitatively.

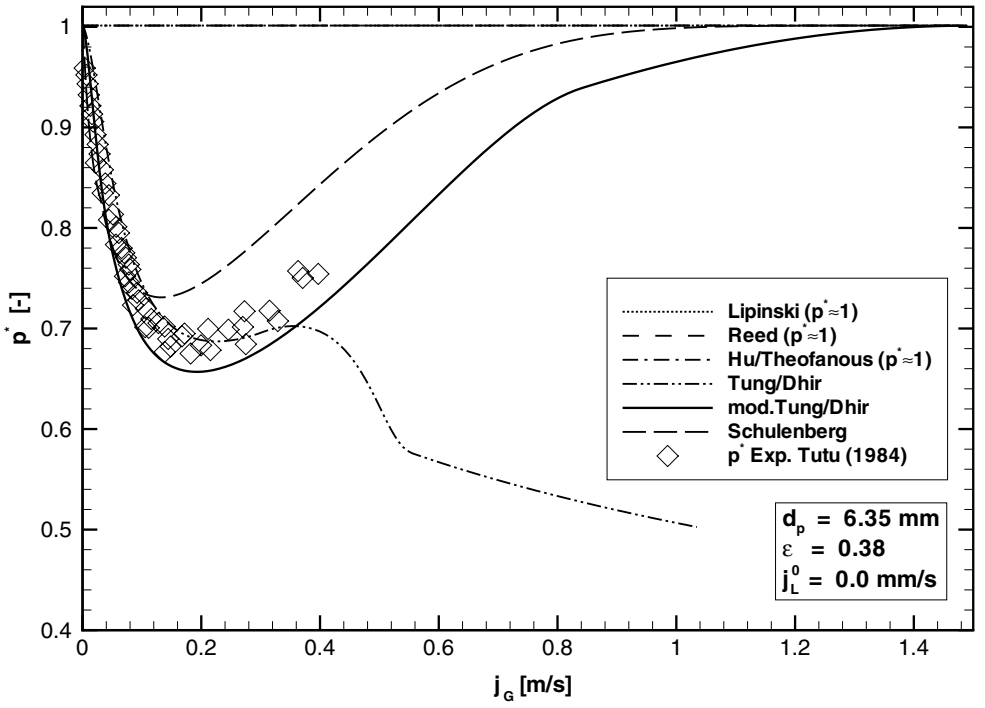

Fig. 3. Dimensionless pressure gradient $P^{\star}$ for an isothermal air/water experiment with no net water flow.

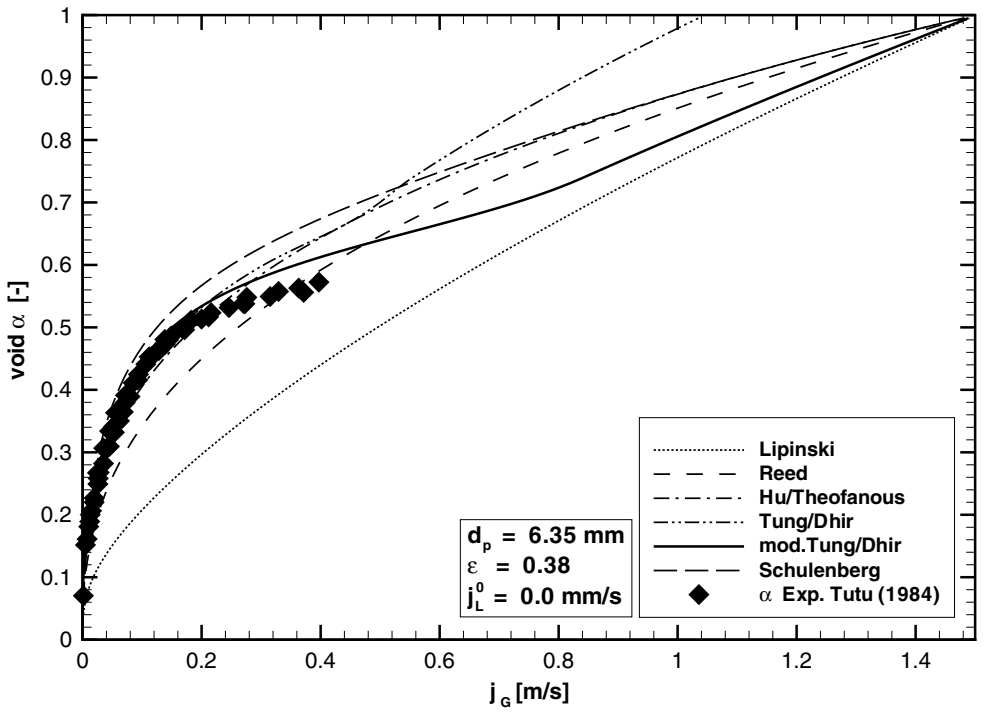

Fig. 4. Void fraction α in the case of Fig. 3.

As already mentioned in the last chapter, the interfacial friction law in the annular flow regime of the Tung/Dhir model has to be modified to obtain a reliable trend for large voids up to one. This can also be seen in Fig. 3. With increasing gas flow rate, the pressure gradient first strongly decreases below the hydrostatic one due to the drag of the up-flowing gas bubbles and slugs on the liquid. Later, with further increased gas flow, the friction between the phases decreases again for void fractions greater than 0.5, as the interfacial area between the gas and the water decreases. This explains the increase in the normed pressure gradient for higher gas fluxes. A limit is reached when the gas replaces all the water. This is the case when the pressure loss due to the gas flow is equal to the hydrostatic head of the water, independent of the model. This limit is not reached for the original Tung/Dhir model. To compensate this, it was proposed in the previous chapter to multiply the interfacial friction by $(1-\alpha)^2$ in the annular flow regime, to get a cubic decrease for large void fractions. The comparison with the experimental data, especially the development for high gas fluxes in Fig. 3, strongly supports this modification of the Tung/Dhir model.

Similar conclusions can be drawn from the corresponding void data in Fig. 4. Although the experimental data points are not up to the annular flow regime, the modified Tung/Dhir model fits the experimental points better. This is due to the decreased bubble diameter in the slug and bubbly flow regime ($D_b = 2.6$ mm modified instead of 3.75 mm in the original form), yielding an increased interfacial friction. Additionally, as already described for the pressure gradient, the tendency in the annular flow regime for the original Tung/Dhir formulation is again not reliable. The one-phase flow limit with $\alpha = 1$ should be reached at the same gas velocity for all models, independent of the interfacial drag. The modified formulation, with decreased interfacial friction in the annular flow regime, fulfills this condition.

For the special case with no net water flow in the porous medium ($j_L = 0$), an enhanced analysis is possible. The interfacial friction can be deduced directly from the measured pressure gradient and void fraction via the liquid momentum equation given in (1). The results for the described data together with the results of the various models are given in Fig. 5 as function of the void fraction. While the interfacial friction is always zero for the classical models, a principle agreement of the enhanced models with the experimental data can be seen. But, especially the local maximum at higher void (higher j_G) in the original Tung/Dhir formulation seems to be not verified by the experiment. This bump originates in the annular flow regime. Furthermore, as already

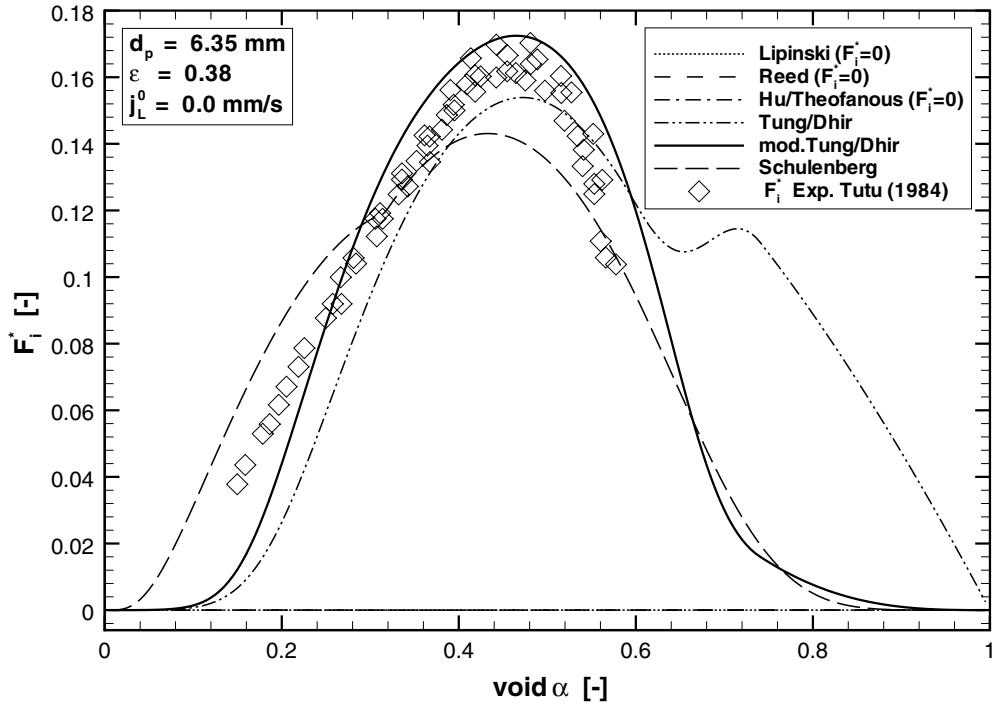

Fig. 5. Experimentally and theoretically deduced dimensionless interfacial friction in the case of Fig. 3.

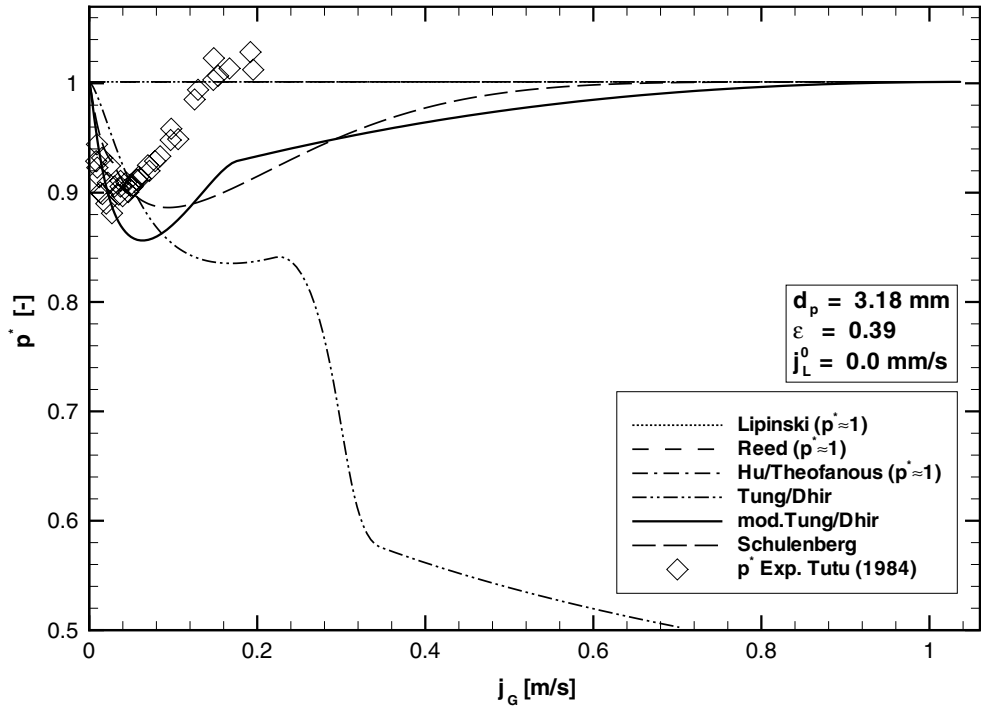

Fig. 6. Dimensionless pressure gradient $P^{\star}$ for an isothermal experiment filled with smaller particles ($d_p = 3.18$ mm).

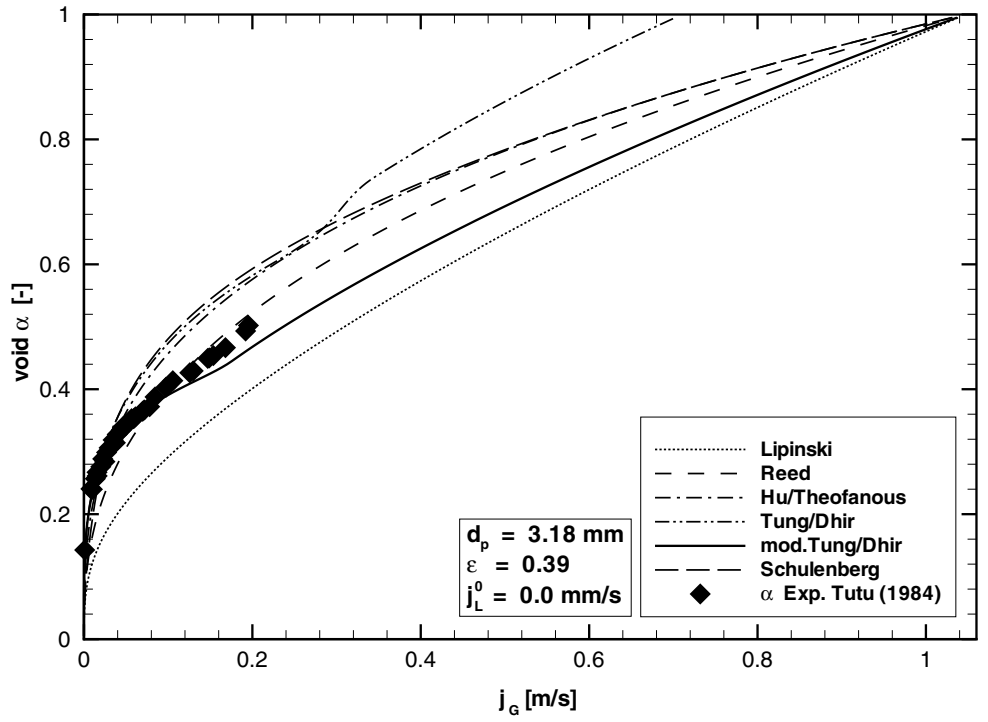

Fig. 7. Void fraction α in the case of Fig. 6.

mentioned, the linear decrease of $F_i^{\star}$ for $\alpha \to 1$ is unreliable. These faults are eliminated by the modifications of the Tung/Dhir model proposed in Section 2.2.3, which then yields the best estimate for the experimental data.

Measurements for larger particles with a diameter of $d_p = 9.9$ mm (Chu et al., 1983) and $d_p = 12.7$ mm (Tutu et al., 1984) yield similar results. A comparison of the experimental data with the different models is given in Schmidt (2004).

For smaller particle diameters, which are to be expected during a severe accident in a nuclear power plant, the models show greater deviations compared to the experimental data. Results of Tutu et al. (1984) for $d_p = 3.18$ mm are given in Figs. 6 and 7. The described modifications of the original Tung/Dhir model – especially the modifications of the flow pattern limits and the modified slug size – are seen to be of decisive influence for smaller particle sizes, e.g. the annular flow regime starts at a void fraction of 0.45, while the pure bubbly flow disappears. This is obviously plausible because the pores are too small for the bubbles.

The influence of the interfacial friction is plotted in Fig. 6. Again, the decrease in the pressure gradient with increasing gas flow rate is only reproduced by the enhanced models including the interfacial friction explicitly. But the further measured increase for higher gas fluxes is steeper than expected from these models. Looking additionally at the void development, only the modified Tung/Dhir model yields satisfying results. This can be seen even better for the interfacial friction, given in Fig. 8. Especially for voids greater then $\alpha = 0.5$ the measured interfacial drag is zero. This can only be explained in the flow pattern picture with the transition to a channel-like configuration with only minor contact of gas and water, as described by Haga et al. (2000). The interfacial friction is significantly reduced because of the smaller interfacial area in this flow pattern. In the modifications to the Tung/Dhir model proposed in the previous chapter, this reduction is included in the redefined lower limit for the annular flow regime and in the reduction of the interfacial friction with decreasing particle diameter. As such small particulate debris has to be expected during a severe accidents in a nuclear power plant the modifications gain importance in the application.

Chu et al. (1983) also performed corresponding experiments with a net water flow in co-current as well as in counter-current configuration. The co-current results, with water and air injection into the bottom, confirm the above results in principle. As an example, results for a fixed water superficial velocity are given in

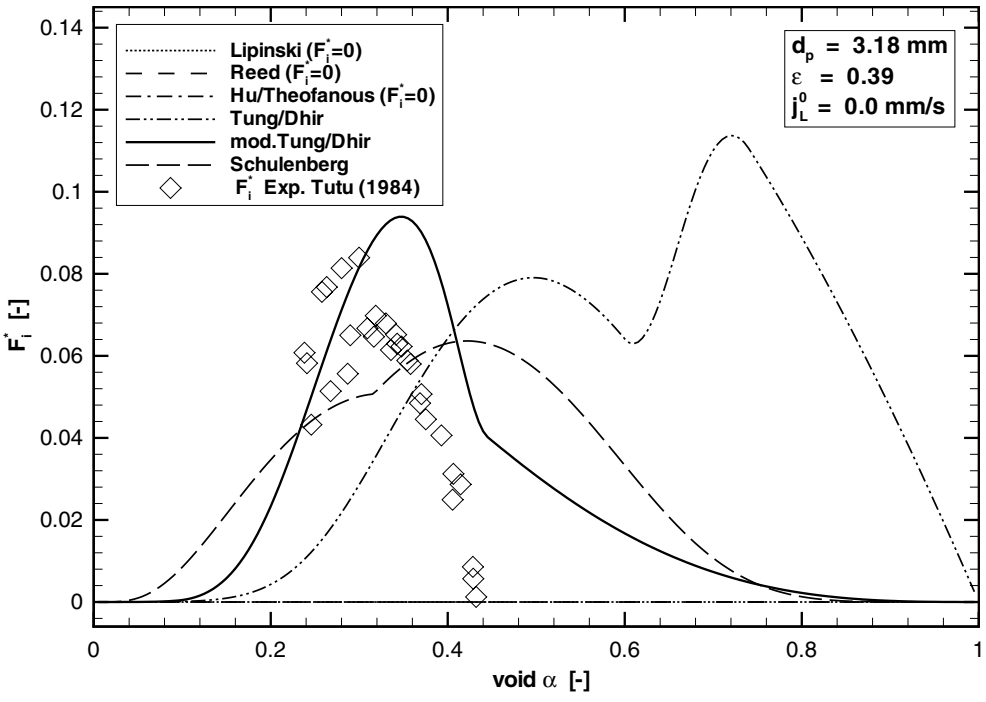

Fig. 8. Experimentally and theoretically deduced dimensionless interfacial friction in the case of Fig. 6.

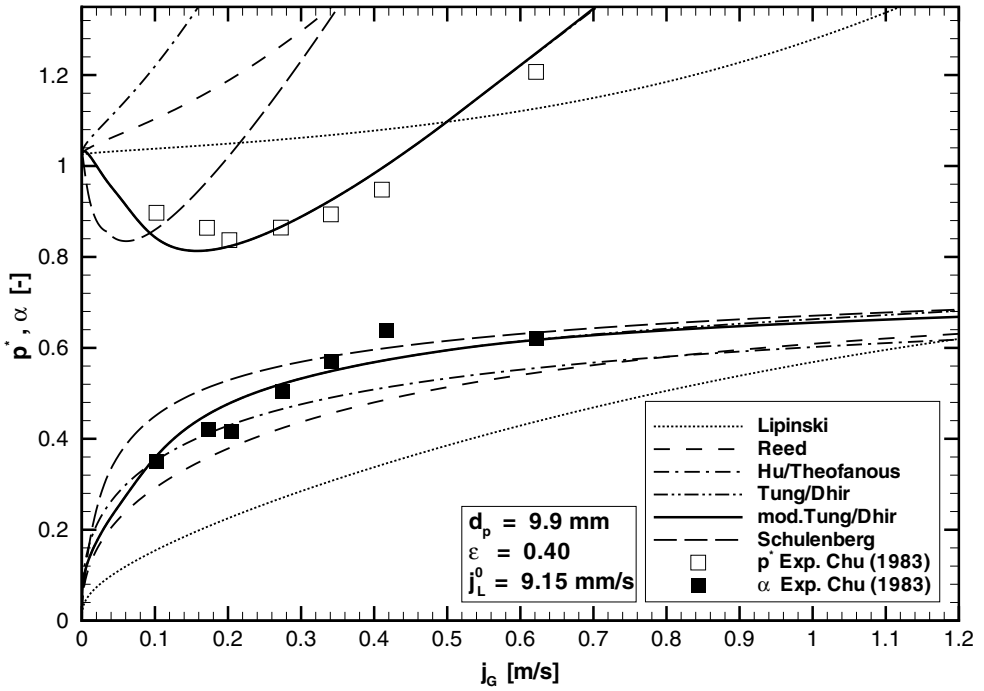

Fig. 9. $P^{\star}$ and α for co-current air/water flow with constant water flow rate.

Fig. 9. As, per definition, the net water flow is fixed, the void limit of $\alpha = 1$ cannot be reached in this case. Increasing the gas mass flux yields an increasing pressure gradient, that presses the fluids through the porous structures, as can be seen in Fig. 9.

More interesting with respect to debris coolability is the counter-current flow configuration, where water is added to the top and exhausted from the bottom of the test section, yielding a top to bottom flow. Then, the bottom injected gas and exhausted water are in counter-current mode, similar to the case of a boiling bed with a coolant pool on the top. Again, for fixed water mass flux, the air inlet rate is varied. Results of the measured pressure gradient and void fraction, as well as the corresponding theoretical results are given in Fig. 10. In contrast to the co-current case, an upper limit for the gas superficial velocity exists, corresponding to a maximum gas mass flux. This limit is the counter-current flooding limit. No larger gas fluxes than this limit are possible in such a configuration. From Fig. 10 it can be seen that this value corresponds to a maximum void fraction. This fraction cannot be 1, because a certain amount of the cross-section or volume is necessary for the water flow. A further increase of the gas flow rate is not possible because this would hinder the water flow.

3.2. Comparison to experiments with boiling debris beds

In contrast to the isothermal air/water experiments, the local flow rates vary inside a boiling bed, even in a one dimensional configuration. The local gas flux, driven by buoyancy forces, is determined by the integrated steam flux, and thus by the bed power integrated from the bottom. For a homogeneous power distribution the steam mass flux is given by $\varrho_G j_G(z) = Qz/\mathrm{LH}$, where Q is the volumetric power density and $\mathrm{LH} = h_G - h_L$ is the specific latent heat of the evaporation. In a steady state the corresponding local water flux is directly given by the mass conservation equation. Assuming water inflow just from a pool above the bed, the liquid mass flux follows from $\varrho_L j_L(z) = -\varrho_G j_G(z)$.

The dryout heat flux of 1D boiling debris corresponds to the counter-current flooding limit. This limit is reached near the top, where the steam flux as well as the downflowing water flux are highest. The friction at this bottleneck – the location of highest steam fraction – is decisive for the coolability of the whole bed.

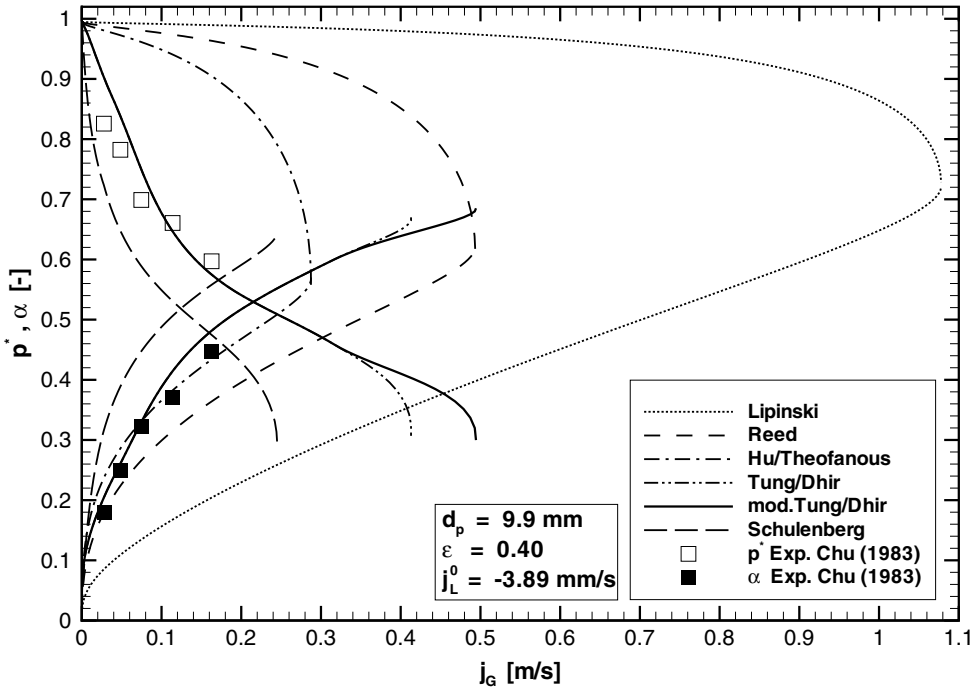

Fig. 10. $P^{\star}$ and α for counter-current air/water flow with constant water flow rate.

3.2.1. The DEBRIS experiment

For specific investigations of the exchange terms, the friction laws, as well as the heat transfers in boiling particulate beds, experiments have been carried out in the DEBRIS facility at IKE, University of Stuttgart (Schäfer, 2003). A sketch of the experimental setup is shown in Fig. 11. A ceramic cylinder of 12.5 cm diameter and a height of 60 cm is filled with oxidised steel spheres. These particles are heated inductively to represent the decay heat. The power distribution is almost homogeneous. Sixty-four thermo-elements are distributed in the test column to detect local dryout. Along the bed height, eight pressure tubes are connected to differential pressure transducers to allow pressure gradient measurements at seven different levels. The coolant flowing into the porous region comes from a water pool above the bed. Optionally, an adjusted water inflow rate from below can be injected. With this facility dryout experiments, as well as experiments on quenching of dry, hot particles are possible.

Besides the direct measurements of the dryout heat flux by increasing the bed power until the first local temperature raise is detected, experiments with steady states in boiling beds can be used to deduce the friction laws. The produced upflowing steam accumulates from bottom to top while the evaporated water has to be replaced by water inflow. So, for a steady state the water and steam fluxes at each level are defined by the total power below. The measured pressure gradients can again be used to compare the various friction models with the experimental data. All the measured values for different heating power can be collected in one plot. Fig. 12 shows the experimental data for 6 mm particles at a pressure of 1 bar. The pressure gradient, adjusted by the hydrostatic head of water, is shown versus the superficial velocity of the steam j_G. Because of the statistical character of the measurements, an error in the order of 500–1000 Pa/m has to be assumed for the experimental data.

Additional to the superficial velocity of the steam j_G the corresponding superficial liquid velocity j_L is given as second x-axis in the plots. In the top part of Fig. 12 the results for a pure top fed configuration are shown. Here, the steam and the water fluxes are always in counter-current mode, as can be seen by comparing the different x-axes. With fixed water injection from the bottom, co-current mode occurs in lower particle bed regions, as can be seen on the j_L-axis in the lower part of the figure.

In addition to the experimental data, results of calculations based on the different models for the given conditions are also plotted in Fig. 12. In principle, the development of the pressure gradient shows the same

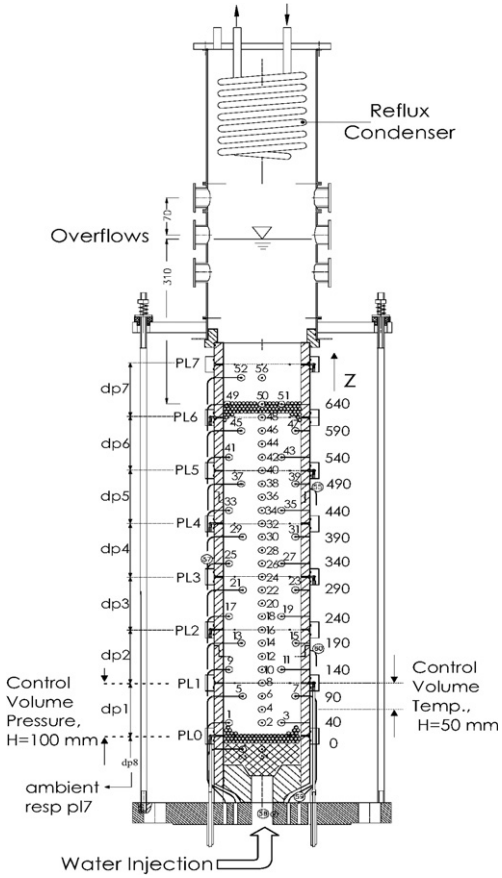

Fig. 11. DEBRIS experimental setup.

behaviour as in the counter-current air/water flow of Fig. 10. Again, it can be seen that the classical models without interfacial friction cannot reproduce the experimental data, and thus must be rejected. Only the enhanced models, including an explicit formulation of the interfacial drag, fit qualitatively to the experimental results.

Many data points have been measured for small vapour velocities. In this range, the enhanced models show no remarkable difference. For higher gas fluxes, where stronger difference between the models can be seen, it was difficult to establish steady states. So, only a few data points with a larger spread could have been measured in this range. Based on this data alone, no final conclusion can yet be drawn to finally prove the model formulations.

The development of the classical models to obtain the measured dryout heat flux, corresponding to the maximum j_G, can also be seen in the figure. The first approach from Lipinski yields a dryout heat flux higher than measured for top cooled particulate beds. By increasing the friction in the relative passability, as done by Reed, the measured critical heat flux was better reproduced. In Fig. 12 this can be seen by the smaller maximum reachable gas velocity. As already mentioned, Hu and Theofanous (1991) criticised the published dryout heat flux data due to the measuring procedure, and consequently introduced even stronger particle fluid friction. This adaptation process can also be seen in the isothermal air/water experiments as in Fig. 10. But, looking at the pressure gradient development, one sees that this adjustment does not represent the measured pressure losses. These can only be explained by including the interfacial friction, just as in the case with no net water flow.

In principle, the results with water fed from below show the same behaviour, as can be seen in the lower plot. The pressure field obtained by the enhanced models again shows the basic behaviour. These models fit well in both configurations, the counter-current ($j_L < 0$) as well as the co-current flow ($j_L \geqslant 0$).

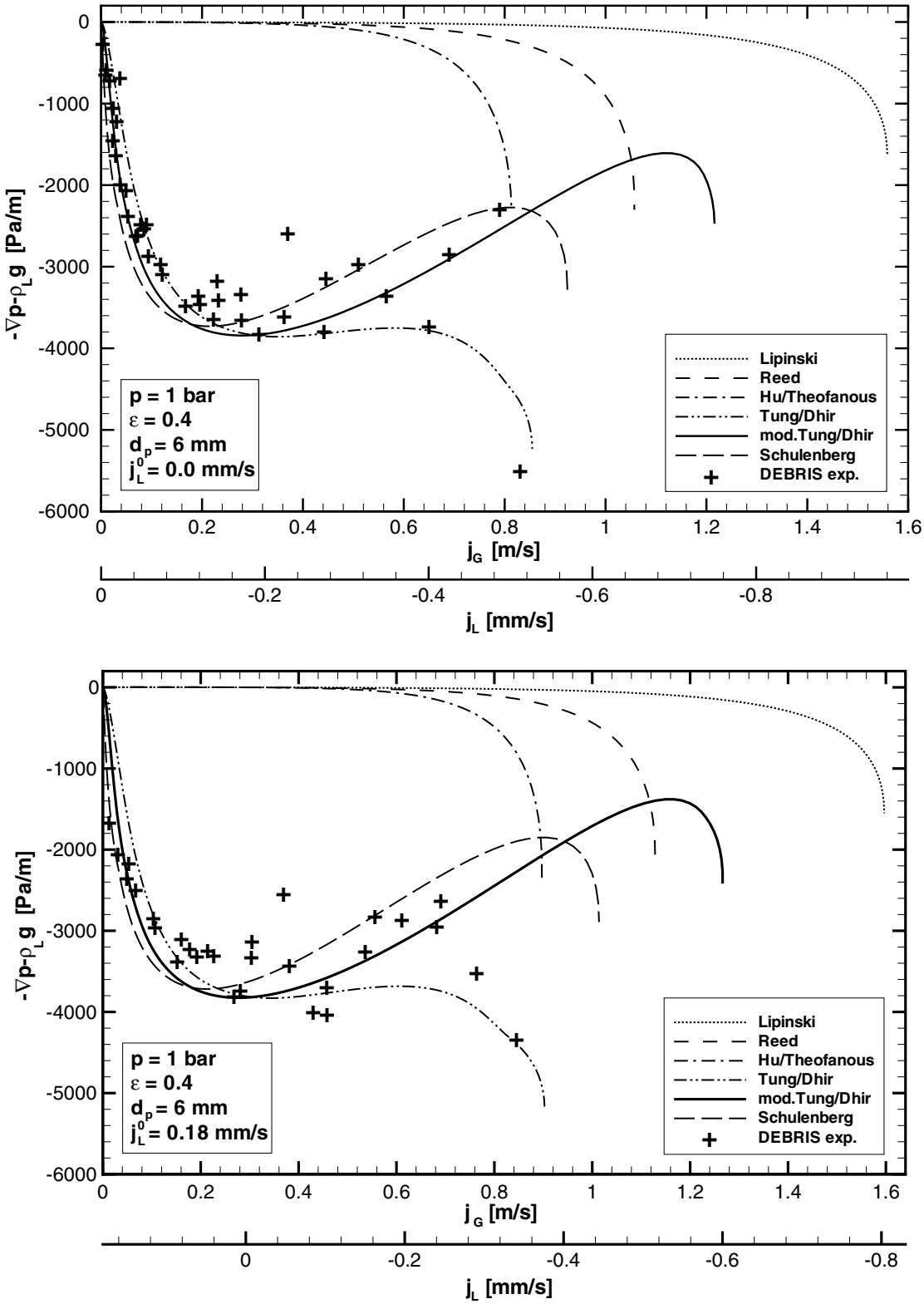

Fig. 12. Pressure gradient in steady states in the DEBRIS experiments for $d_p = 6$ mm (top: without water injection from below; bottom: with water injection from below).

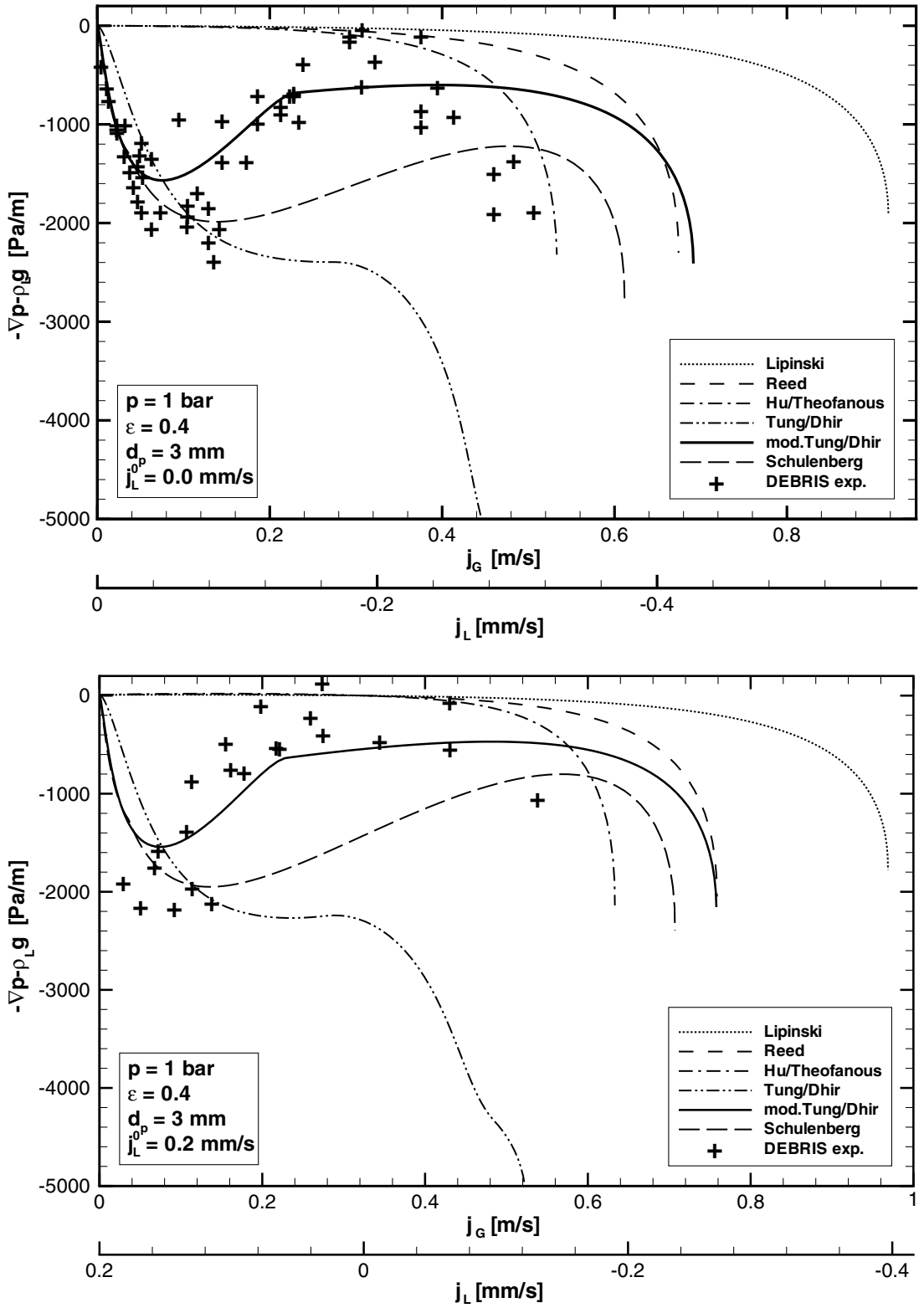

Fig. 13. Pressure gradient in steady states in the DEBRIS experiments for $d_p = 3$ mm (top: without water injection from below; bottom: with water injection from below).

Data of analogous measurements with smaller particles with $d_p = 3$ mm are given in Fig. 13 together with the results of the models. The subfigure on the top again is for a pure top fed configuration, while the lower plot shows the results with a small water inflow of $j_L = 0.2$ mm/s from below. This yields data points in co-current as well as in counter-current mode. As was already seen for the isothermal experiments in the previous section the modifications to the Tung/Dhir model proposed in Section 2.2.3 gain importance for such small particles. This can be seen when comparing the calculated results of the modified with the ones of the original formulation. While the original Tung/Dhir model yields a steady decrease of the pressure gradient with increasing vapour flux, the modified formulation also shows the interim increase due to the reduced interfacial drag in the annular flow regime and fits the measured data well. This behaviour is also predicted by the Schulenberg model. But again, due to the spread in the experimental data, no final conclusion can be drawn on which of the these two models is the better one.

3.2.2. Application to DHF experiments

Various experimental programs for direct investigation of the dryout heat flux for volumetrically heated porous structures were performed, especially at the beginning of the 1980s. In most of these experiments the particulate debris consists of inductively heated metallic spheres in a one-dimensional test column. Some authors used real granular particle beds and applied direct electrical resistance heating (e.g. Hu and Theofanous, 1991) or heated the particles by irradiation (e.g. DCC experiments, Reed et al., 1985). The coolant, mostly water, infiltrates from a pool at the top. Under these conditions the first dryout has to be expected after a very slow transient slightly above the limiting bed power near the bottom of the test column.

Results of measurements for the commonly used conditions described above can directly be compared for different parameters. The dryout heat flux versus the particle diameter measured by various authors for a system pressure of 1 bar is shown in Fig. 14 together with results of the different friction models. In general, it can be seen that the different experiments yield some spread in the published data. This is due to different experimental setups and measurement procedures. In the models, the dryout heat flux corresponds to the counter-current flooding limit and, therefore, depends on the drag at this limit, as already discussed. A general statement on the validity of the models only based on these values is not possible. However, the tendency to

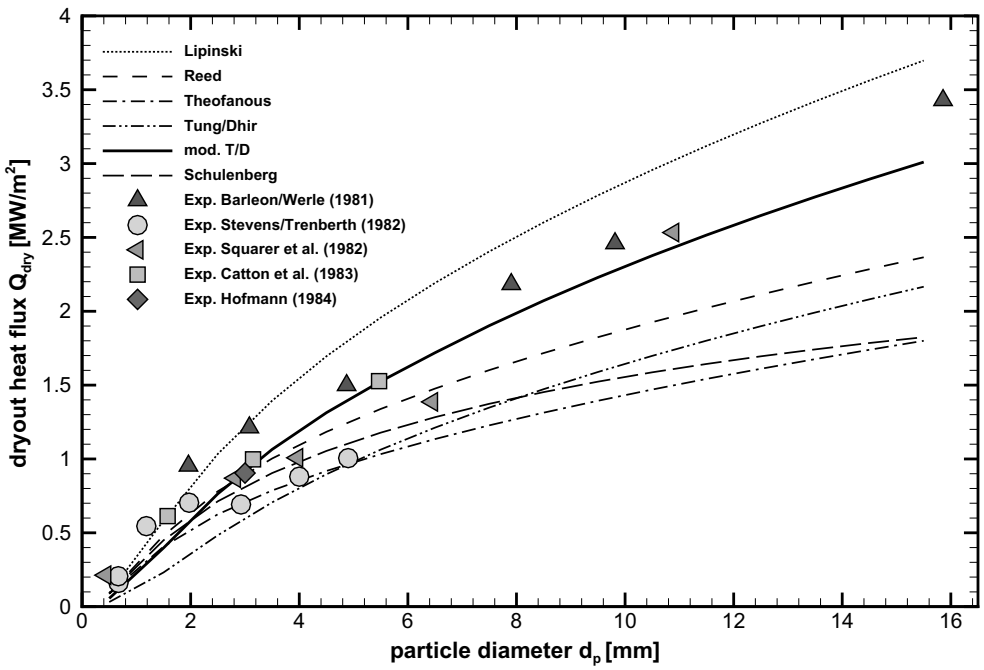

Fig. 14. Dryout heat flux in top fed beds for different particle diameters (Barleon and Werle, 1981; Squarer et al., 1982; Catton et al., 1983; Hofmann, 1984).

yield smaller dryout heat fluxes can be seen with increasing friction in the classical models from Lipinski over Reed to Theofanous. While the commonly used Reed model looks good for small particles, the measured DHF values are higher than predicted for larger particles. A good representation of the data over the whole range is again given by the modified Tung/Dhir model. So, these results support again the modifications proposed in Section 2.2.3.

For configurations with enhanced coolant inflow possibilities, the dryout heat flux will increase. In a pure 1D setup, as sketched in Fig. 1b, inflow from below is favoured, because the small void fractions there yield a reduced coolant-particle friction. Additionally the coolability is supported by the drag of the up flowing steam. In contrast to the top fed case, the dryout will now not occur at the bottom. The evaporated water for a main part of the bed will be replaced by inflow from below, and only some fraction may infiltrate from the top pool. The up-flowing water will be evaporated on its way up to a level where all is spent. Only the region above this level is cooled from above and may be regarded as a top fed configuration with gas inflow from below.

The inflow rate from below is determined by the pressure gradient at the bottom and thus by the pressure in the porous media. This pressure field strongly depends on the drag terms and thus on the model formulation. To catch both situations, the co- and the counter-current mode the interfacial drag has to be considered explicitly in the model.

Only two experiments with such inflow conditions are known. Stevens and Trenberth (1982) used spheres with a diameter between 0.126 mm and 5 mm while Hofmann (1984) used only a particle diameter of 3 mm. These experiments show an increase of the dryout heat flux by a factor between 1.5 and 3. The measured values are given in Fig. 15 together with results of the different models. The first point to be noticed is valid for all models. Compared to the top fed case the dryout heat flux is increased because of the facilitated water inflow from below, as expected. Hofmann's data in particular shows a much stronger increase than calculated by the classical models. The interfacial drag in the enhanced models additionally favours the water inflow from below, while hindering it from the top. Here the influence of the bottom inflow is much stronger.

A summary of calculated results of the different models for a particle diameter of $d_p = 3$ mm, corresponding to the Hofmann experiment, is given in Table 3. As can be seen, the ratio of bottom to top dryout heat flux (DHF_{bottom}/DHF_{top}) is more pronounced for the enhanced models. For these, almost all water evaporated in the particle bed is replaced by inflow via the bottom into particulate bed. This can be seen in the table at the

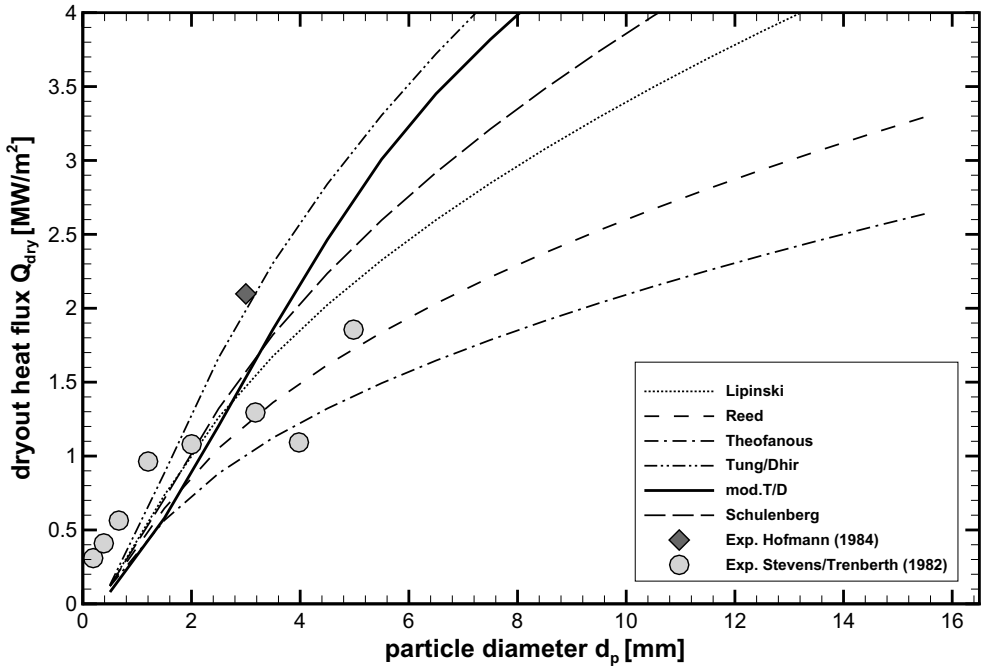

Fig. 15. Dryout heat flux in particle beds with bottom water inflow driven a hydrostatic head for different particle diameters.

Table 3
Theoretical dryout heat flux for top and bottom fed configurations with $d_p = 3$ mm

	L	R	T	TD	mTD	S
Dryout heat flux (top fed) [MW/m^2]	1.22	0.90	0.71	0.60	0.93	0.82
Dryout heat flux (top/bottom fed) [MW/m^2]	1.48	1.22	1.01	2.00	1.42	1.58
DHF_{bottom}/DHF_{top}	1.21	1.35	1.42	3.34	1.53	1.94
Flow rate from below (j_L [mm/s])	0.564	0.454	0.374	0.925	0.642	0.725
Level fed from below (%)	0.825	0.807	0.801	0.999	0.976	0.990

L: Lipinski; R: Reed; T: Theofanous; TD: original Tung/Dhir; mTD: modified Tung/Dhir; S: Schulenberg.

level that is fed from below. The gain in coolability is most significant for the original Tung/Dhir formulation, but this is also affected by the very low top fed value. For the top fed configuration Hofmann reported a dryout heat flux of $q_{dry} = 920$ KW/m^2. Comparing this with Table 3 it has to be noted that Reed, for the classical models, and Schulenberg as well as the modified Tung/Dhir formulation yield satisfying results. But, the value for additional bottom inflow is better reached for the enhanced models. In general, it is not possible to tune the particle-fluid drags in the models without interfacial friction to fit the top as well as the bottom fed configuration. So, the interfacial drag has to be modeled explicitly. A better experimental basis of such investigations is necessary for the validation of the enhanced models.

4. Summary and conclusion

The measured pressure loss in the isothermal air/water flow experiments as well as for boiling porous structures can only be explained by explicit consideration of the interfacial drag. Simpler models, as those classically used for the analysis of the coolability of particulate debris with internal heat sources, are insufficient for calculating the pressure field. Especially for multidimensional configurations with flow paths to lower regions the pressure field directly influences the coolant supply. Thus, there is a direct feedback between the pressure field and the coolant influx.

In general, the separation of the friction contributions from the solid matrix and from the other fluid phase is not possible. Only in the case when gas is sparging through a liquid filled porous structure can the interfacial drag be determined. In the general case with flowing liquid and gas, all friction terms together determine the pressure loss and thus the pressure field.

Based on the experiments an enhanced model based on a formulation according to Tung and Dhir was proposed in this paper. As described, the flow pattern limits have to be modified for small particles. Additionally, the formulation of the interfacial drag in the annular flow regime was modified to reach a reliable limit for high voids. This modified model fits the experimental data well.

In the application field of nuclear reactor safety, the coolability of fragmented corium by evaporation of water is of central concern. Multidimensional configurations with flow paths to lower regions determined by the settling of the particles or geometric conditions have to be assumed. The amount of water that infiltrates through these flow paths into the particle bed depends on the internal pressure field, and thus on the friction terms. Especially the interfacial drag between the produced steam and the water is decisive. The interfacial friction supports water inflow to bottom regions while it hinders the direct infiltration from the top. Applications of the models given here for realistic configurations can be found in Schmidt (2004).

Acknowledgement

This work was accomplished at the Institut für Kernenergetik und Energiesysteme (IKE), University of Stuttgart, Germany.

References

Barleon, L., Werle, H., 1981. Dependence of dryout heat flux on particle diameter for volume- and bottom-heated debris beds. Technical Report KfK 3138, Kernforschungszentrum Karlsruhe.

Catton, I., Dhir, V.K., Somerton C.W., 1983. An experimental study of debris-bed coolability under pool boiling conditions. Technical Report EPRI NP-3094, University of California at Los Angeles.

Chu, W., Dhir, V.K., Marshall, J., 1983. Study of pressure drop, void fraction and relative permeabilities of two phase flow through porous media. In: Heat transfer – Seattle, AIChE Symposium series, vol. 79, pp. 224–235.

Ergun, S., 1952. Fluid flow through packed columns. Chem. Eng. Prog. 48, 89–94.

Haga, D., Niibori, Y., Chida, T., 2000. Tracer responses in gas–liquid two-phase flow through porous media. In: Proc. World Geothermal Congress, Kyushu – Tohoku, Japan.

Hofmann, G., 1984. On the location and mechanisms of dryout in top-fed and bottom-fed particulate beds. Nucl. Technol. 65.

Hu, K., Theofanous, T., 1991. On the measurement and mechanism of dryout in volumetrically heated coarse particle beds. Int. J. Multiphase Flow 17.

Lipinski, R., 1981. A one dimensional particle bed dryout model. ANS Trans. 38, 386–387.

Lipinski, R., 1984. A coolability model for postaccident nuclear reactor debris. Nucl. Technol. 65, 53–66.

Reed, A., 1982. The effect of channeling on the dryout of heated particulate beds immersed in a liquid pool. PhD thesis, Massachusetts Institute of Technology, Cambridge.

Reed, A., Boldt, K.R., Gorham-Bergeron, E.D., Lipinski, R.J., Schmidt, T.R., 1985. DCC-1/DCC-2 Degrated Core Coolability Analysis. Technical Report NUREG/CR-4390, SAND85-1967, Sandia National Laboratory.

Schäfer, P., Steiner, D., Groll, M., Kulenovic, R., Schmidt, W., Bürger, M., Widmann, W., 2003. Wechselwirkung Debris/RDB-Wand: Analytische und experimentelle Untersuchungen zur Külbarkeit und Rückhaltung verlagerten Kernmaterials (Debris) im unteren RDB-Plenum eines LWR. Technical report IKE 5TB-1751-013, IKE, Universität Stuttgart.

Schmidt, W., 2004. Influence of Multidimensionality and Interfacial Friction on the Coolability of Fragmented Corium. Ph.D. Thesis, Institut für Kernenergetik und Energiesysteme, Universität Stuttgart. ISSN-0173-6892.

Schulenberg, T., Müller, U., 1986. A refined model for the coolability of core debris with flow entry from the bottom. Proc. of the Sixth Information Exchange Meeting on Debris Coolability. In: EPRI NP-4455. University of California, Los Angeles.

Squarer, D., Pieczynski, A.T., Hochreiter, L.E., 1982. Effect of debris bed pressure, particle size and distribution on degraded nuclear reactor core coolant. Nucl. Sci. Eng. 80, 2–13.

Stevens, G., Trenberth, R., 1982. Experimental studies of boiling heat transfer and dryout in heat generating particulate beds in water at 1 bar. In: Proc. of the Fifth Post Accident Heat Removal Information Exchange Meeting. Nuclear Research Center, Karlsruhe.

Tung, V.X., Dhir, V.K., 1988. A hydrodynamic model for two-phase flow through porous media. Int. J. Multiphase Flow 14, 47–65.

Tutu, N., Ginsberg, T., Chen, J., 1984. Interfacial drag for two-phase flow through high permeability porous beds. J. Heat Transf. 106, 865–870.